Engineering Science and Technology, an International Journal 41 (2023) 101403

HOSTED BY

Contents lists available at ScienceDirect

Engineering Science and Technology, an International Journal

journal homepage: www.elsevier.com/locate/jestch

FEM-based optimal design and testing of synchronous magnetic coupling for aerospace Starter/Generator applications

Sami Arslan [a,*], Ires Iskender [b], Tuğba Selcen Navruz [c]

[a] Electrical and Electronics Engineering Department, Gazi University, Graduate School of Natural and Applied Sciences, Ankara 06500, Turkey
[b] Electrical Electronics Engineering, Çankaya University, Ankara 06790, Turkey
[c] Electrical and Electronics Engineering, Gazi University, Ankara 06560, Turkey

ARTICLE INFO

Article history:
Received 29 August 2022
Revised 6 March 2023
Accepted 24 March 2023
Available online 4 April 2023

Keywords:
Contactless power transmission
Optimisation
Parametric solution
Radial magnetic couplers
Synchronous couplings

ABSTRACT

Improvements in high energy density rare-earth permanent magnets make it innovative to develop magnetic couplings for Starter/Generator applications in the light of more electric aircraft to ensure magnetically insulated contactless power transmission between decoupled shafts for safe operation. Although there are essential studies on magnetic couplings in the literature, especially those for aerospace Starter/Generator structures are rarely encountered. However, methodologies considering system constraints and examining design parameters of couplings are in demand. In response to such a need, this paper proposes the novel design of highly reliable synchronous radial magnetic couplings with torque requirements of 6 and 12 N·m to isolate Starter/Generator and piston engine shafts in model aircraft. The preliminary volume is obtained analytically. Simulations are executed by optimetric approaches in Ansys Maxwell 2D. Optimisation techniques are compared in Maxwell 3D to get the final shape. The retaining sleeve of 0.5 mm is suggested. Loss of synchronisation in the event of the piston shaft failure or exceeding the maximum torque of the coupling is also examined. The torque fluctuation at load changes is 0.1%. Performance tests are conducted on the direct dynamic test bench. Absolute error margin is 37% for the Virtual Work method, 13% for 2D FEM and 6% for 3D FEM. The coupling efficiency is 93.8% at the maximum operating speed and the critical angle, and 96.9% at the minimum torque angle and the minimum operating speed.

1. Introduction

In recent years, the desire for rapid developments in the aviation industry to increase efficiency and safety has started the more electric aircraft initiative [1]. In this sense, piston-engined Unmanned Aerial Vehicles (UAVs) need renovation to use more efficient electrical systems that will increase reliability and endurance, avoiding heavy mechanical mechanisms. This modernisation makes it necessary to integrate Starter/Generator structures into developing aviation systems.

Piston Engines (PEs) which are prevalent in propulsion systems and require the first actuation movement, are internal combustion engines that convert heat energy into motion energy. A Starter/Generator (S/G) is a unique and efficient rotary electric machine in which the same device can operate as both a motor and a generator so that the piston engine is driven first in motor mode, and the battery group is charged in generator mode while cruising [2]. The S/G is capable of an out-runner or in-runner rotor topology, depending on the application [3].

Unfortunately, in conventional systems, due to the propeller being connected directly to the piston engine, any shaft failure causes the aircraft to crash. Significant efforts to prevent these damaging situations have led to the use of Magnetic Couplings (MCs) both for noncontact torque transfer and to magnetically isolate the shafts of the PE and the S/G. In this way, in case of any malfunction, the S/G will operate in motor mode, ensuring a safe landing of the aircraft on the ground.

The MC consists of inner and outer rotors, Permanent Magnets (PMs), and a retaining sleeve as the main parts, while the subparts are the case, shaft, static seal shrould, and flanges. It is classified according to the interaction type of the magnetic field [4], as shown in Fig. 1.

Synchronous magnetic couplings, as shown in Fig. 1(a), have permanent magnets inserted on both sides or one half-side. In contrast, asynchronous magnetic couplings only have PMs on one side and conductive or hysteresis material on the other, as shown in Fig. 1(b). Unlike eddy current and hysteresis couplings,

* Corresponding author.
E-mail address: sami.arslan1@gazi.edu.tr (S. Arslan).

https://doi.org/10.1016/j.jestch.2023.101403
2215-0986/

Fig. 1. Coupling types of (a) Synchronous (active) (b) asynchronous (eddy current).

synchronous couplings have no slippage between the inner and outer rotors. Further classification as the magnetisation direction of permanent magnets is carried out as radially magnetised and axially magnetised.

Recently, a significant amount of work has been done on magnetic coupling design in different ways. These studies come across two different approaches, analytical and numerical.

Yonnet *et al.* [5] developed an analytical method for torque calculation of synchronous couplings based on the forces between permanent magnets. Ravaud *et al.* [6] offered analytically approached three-dimensional expressions for optimising permanent magnet couplings based on the Coulombian model. Choi *et al.* [7] showed the torque analysis and measurements of cylindrical air–gap synchronous permanent magnet couplings based on analytical magnetic field calculations. These studies have not comparatively investigated the coupling parameters affecting the transmitted torque.

However, numerical methods using finite elements [8–10] provide more realistic solutions, although they extend the solution time. Therefore, they are more efficient in achieving the optimum design and the applicability of optimisation techniques. Baiba-Ose and Vladislav Pugachov [11] investigated the influence of permanent magnet width and the number of pole pairs on the mechanical torque of magnetic couplers. Sun *et al.* [12] presented a computational model for cylindrical permanent magnet couplings based on the magnetic field division method, considering both the skin effect and the working point of the permanent magnet. Meng *et al.* [13] parametrically analysed and tested a 3D analysis model for calculating the torque of radial magnet couplers based on the Coulombian model. Guoying Meng and Yaohong Niu [14] simulated the transient magnetic field for permanent magnet coupling in different states using Ansys Maxwell 3D software. However, these studies lacked multiapproach examinations of the design parameters. Structural conditions have not been studied. Nevertheless, the retaining sleeve effect and design have not been investigated.

In addition, study [15] compared different magnetic coupling types. At the same time, axially magnetised coupling [16] was performed. Recently, a magnetic gear study has been reported [17] to replace mechanical gears, which takes magnetic coupling technology one step further. Furthermore, inspired by magnetic gears, a magnetic gear-integrated permanent magnet machine [18] has been proposed. The idea of hybrid coupling [19] was developed using magnetic couplings of different topologies in a single structure. In these studies, a static torque test was not performed depending on the torque angle.

Although only a few, the availability of guiding magnetic coupling studies for aerospace applications has also been reported [20–24]. Charpentier *et al.* [25] studied ironless permanent magnet devices as both a coupling and an axial bearing based on magnetic charge theory for naval propulsion. Bojoi *et al.* [26] examined the advantages, constraints, and drawbacks of the more electric engine through a comparison between radial and axial flux PM machines.

However, application-based studies still need to be improved due to the necessity of specifically designed magnetic couplings where design criteria are considered, although some market products are available.

In this study, FEM-based optimal design and verification of customised radial synchronous magnetic couplings are carried out specifically for the model UAV equipped with a 3W-70R2 piston engine, which is shown in Fig. 2(a). The system limitations and constraints are considered in the design steps. The synchronous MC is intended for one-to-one speed requirements. The radial type is preferred among synchronous types due to cylindrical shaft motion. The whole system model includes the outer rotor yoke (1), outer rotor permanent magnets (2), retaining sleeve and air gap (3), inner rotor permanent magnets (4), inner rotor yoke (5), stamp (6), piston engine shaft (7,8), piston engine stationary body (9) and S/G parts (10), as demonstrated in Fig. 2(b).

The main contribution of the paper is to cover the lack of design methodologies for the use of magnetic couplings in aerospace Starter/Generator applications by examining the multiobjective design

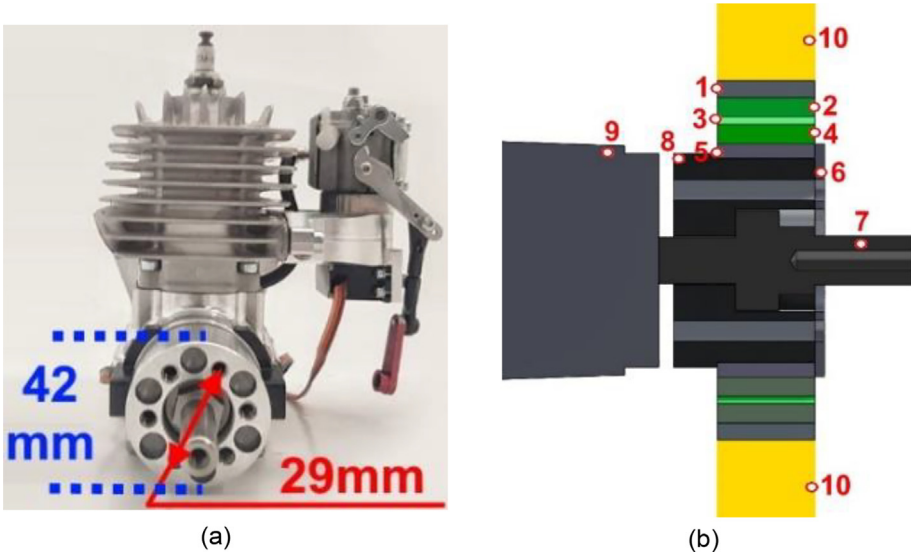

Fig. 2. (a) 3W-70R2 piston engine flange (b) system model with magnetic coupling.

parameters and experimental results in a regular, systematic, and detailed way under a single study. Exploring negative torque to reveal the opposing force in the loss of synchronisation increases the novelty of the paper and sets it apart from other studies. Thus, such negative torque could be considered a safety factor in critical applications such as military aviation. Correction factors for both analytical and numerical methods are proposed separately as a result of the correlation of all the data obtained to achieve good accuracy. This study is notable for the design of a retaining sleeve for the inner rotor of the magnetic coupling.

There are four main contents of this study. Section 2 discusses the design criteria for synchronous radial magnetic couplings. The rotor topologies, materials, and coating types of PM are investigated. The design analyses are considered in detail in Section 3. The models are fully parametrised. Modular design is offered due to outer diameter limitation. Initial sizing is obtained by analytical calculations based on the Virtual Work method. The effect of rotor yokes, magnets, number of poles, and model length is investigated with magnetostatic and transient analyses. Finite Element Analyses (FEA) are performed in Ansys Maxwell 2D with optimetric convergence approaches. The design parameters are then optimised in Maxwell 3D using SNLP, GA, and MOGA techniques. Section 4 presents the experimental results. A direct dynamic test system [27], specially set up for the proposed magnetic couplings, allows static and dynamic performance investigations to be carried out precisely. Unlike other studies, the static torque depending on the torque angle obtained numerically and experimentally contributes to creating a torque transmission capability map of the coupling. Although the experimental outcomes significantly differ from the analytical results, they are in agreement with the FEM outputs. Finally, the results and evaluations are presented in Section 5.

2. Design criteria

Magnetic couplings have significant advantages, such as less maintenance, magnetically isolated protection against overloads, and high tolerance to misalignment between rotors [28]. Most Starter/Generator applications generally have their own limitations. However, typically, the requirement for higher torque density or minimum weight in aviation requires active synchronous-type couplings. The design constraints of the model are listed in Table 1.

The need for the ability to compensate for disturbances such as sudden G-turns and weather-related overloads requires consideration of safety and correction factors. Thus, with the initial selection of safety factor 1.25, correction factor 1.2, and turbulence coefficient 1.1, the required maximum torque for MCs is updated to 10 N·m and 20 N·m, respectively. The maximum torque is also called the pullout torque [13].

On the other hand, the air gap length for analytical and numerical designs is set to 1 mm, excluding the thickness of the retaining sleeve, considering the production capability and the need for sleeve assembly.

Table 1
Design constraints of the magnetic couplings.

Parameter	Value
Maximum torque for MCs, required	6 N·m/12 N·m
Rated operating speed	4000 rpm
Operational speed range	2000 rpm–6000 rpm
Outer rotor outer diameter limitation	74 mm
Maximum model length for MCs	15 mm (for 6 N·m)/25 mm (for 12 N·m)
Total model weight of MCs, max	250 gr (for 6 N·m)/500 gr (for 12 N·m)

2.1. Topology determination of permanent magnets

The necessity of magnetic couplings with relatively high speeds, precisely balanced, easily assembled, lower inertia, and better dynamic response characteristics leads to the choice of a radially oriented permanent magnet topology rather than an axially oriented topology.

Various viable rotor topologies with inherent advantages can be realised [29]. However, due to the ease of fabrication and the need for convenient assembly, a surface-mounted magnet (SMM) with a curved arc type is selected among the feasible options, as shown in Fig. 3.

The outer rotor of the MC, as shown in (1) in Fig. 2(b), is also the rotor of the S/G due to the direct connection of the MC between the PE and S/G shafts, as shown in Fig. 4. This feasibility offers mechanical rigidity without the need for a mounting case for the magnetic couplings, resulting in reduced weight and elimination of torsional loads.

All given dimensions have been verified since the MCs have been prototyped and tested. The objective function is the parameters of MCs with a minimum weight in manufacturable tolerances that meet the requirements defined by the UAV manufacturer.

2.2. Considering the smallest number of poles

The smallest number of poles at which MCs with surface-mounted PMs can operate properly is $2p = 2$, where $2p$ is the number of poles. Increasing the number of poles until a number where high leakages dominate the system will increase the maximum torque [30], but this increase will be limited depending on the permissible outer diameter, operating speed and mounting holes of the coupling.

2.3. Investigation of coupling materials and coating types of PMs

The core materials of the rotors should be selected according to four primary qualifications: saturation level, core losses [31–33],

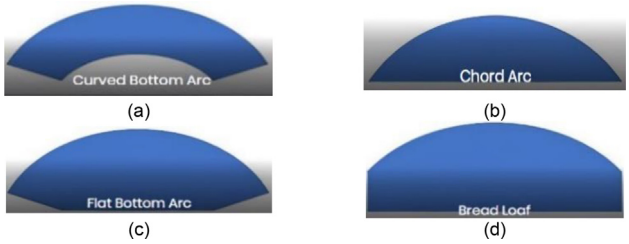

Fig. 3. SMM types (a) curved bottom arc (b) chord arc (c) flat bottom arc (d) bread loaf.

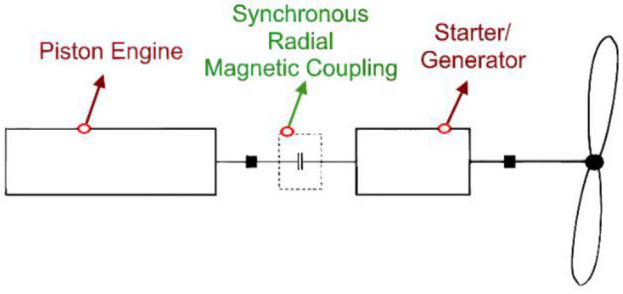

Fig. 4. Connection of magnetic coupling between shafts of PE and S/G.

cost, and manufacturability. Rotor materials that can be used in an industrial sense are Nongrain or Grain Oriented Electric Steel (ES), Carbon Steel (CS), Magnetic Stainless Steel (SS), and Alloy Metals (AM). Although oriented steels have higher magnetic permeability and lower core losses, their commercial availability in sheets complicates their cost and reproducibility. Magnetic stainless steel has lower iron losses and saturation points than carbon steel, but all have similar mass densities. Due to the difficulty of SS and AM in terms of mechanical structure and manufacturability, Steel 1020 is chosen as the rotor material.

Applicable PMs are ferrites, alnicos, and rare-earth magnets, Nd-Fe-B and Sm-Co. Sm-Co magnets work better at higher temperatures than others and in more abrasive environments. Nd-Fe-B has a much stronger magnetic field with the highest B-H_{max}. It is cheaper than Sm-Co and is produced up to thermal class AH (230 °C). Nd-Fe-B is becoming predominant in magnetic couplings due to its high energy density and the absence of a strict temperature constraint associated with the high operating altitude. Neodymium N48H is preferred considering manufacturing and accessibility for design studies. Considering the worst-case conditions and cooling method, dynamic and static simulations are performed at 60 °C and 80 °C, respectively.

However, the retaining sleeve is crucial in protecting the PMs against centrifugal forces at high speeds. Materials such as nonmagnetic steels, carbon fibre, glass fibre, titanium, Inconel, carbon graphite, and reinforced plastics can be used [34]. The nonmagnetic stainless steel sleeve is one of the preferred materials due to its ease of access.

This study aims to investigate the effects of all design parameters of active synchronous magnetic coupling, which provides flexible and safe use in aerospace applications. The dimensioning of the retaining sleeve in terms of its compatibility with the rest of the design was determined accordingly. However, it was not used in dynamic tests due to material supply constraints and production difficulties in prototyping. Therefore, although it is introduced in the Maxwell model, it is not used in the analysis unless otherwise stated. The effect of the sleeve material on loss and torque was also analysed and investigated.

On the other hand, Nd-Fe-B magnets are usually coated against corrosion and rust since they are not inherently corrosion-resistant. The coating also prevents the reduction of the magnetic field caused by the volume loss of the magnet alloy material. Various types of coatings include nickel, zinc, gold, epoxy, plastic, and Teflon. However, the most common type is epoxy for aviation, as marked in red in Fig. 5.

The unique design ability of MCs enables their use in many other industrial areas, such as process engineering [35], water management [36], hydraulic applications [37], compressors and pumps [38].

Plating / Coating	Indoor Use	Abrasion Resistance	Humidity	Water	Salty Air	Salt Water	Glue	Thickness
Nickel (Ni-Cu-Ni)	Excellent	Good	Good	Bad	Bad	Bad	Bad	10-20 Microns
Zinc (Zn)	Excellent	Excellent	Excellent	Good	Good	Bad	Good	8-10 Microns
Gold (Ni-Cu-Au)	Excellent	Good	Good	Bad	Bad	Bad	Bad	10-20 Microns
Black Epoxy (Ni-Cu-BE)	Superior	Bad	Superior	Superior	Excellent	Excellent	Good	15-25 Microns
Raw Epoxy (BE)	Superior	Good	Superior	Superior	Excellent	Excellent	Superior	10-20 Microns
Plastic (ABS)	Superior	Superior	Superior	Superior	Superior	Superior	Excellent	>800 Microns
Teflon® (PTFE)	Superior	Superior	Superior	Superior	Superior	Superior	Bad	250-500 Micron
Everlube-6155®	Superior	Superior	Superior	Superior	Superior	Superior	Good	8-25 Microns

Fig. 5. Nd-Fe-B coating/plating [*see https://www.amazingmagnets.com*].

3. Design analyses

Analytical methods are a fast design tool, although they suffer from lower accuracy [5]. Therefore, they are more helpful in estimating initial dimensions. On the other hand, Ansys Maxwell 3D FEA handles three-dimensional electromagnetic fields and eliminates the use of experiential factors but needs a long solution time. Maxwell 2D FEA provides a faster solution time than Maxwell 3D but neglects the end leakage effects that increase the error. Moreover, a practical constant called the correction factor has been proposed as the basis of the aspect ratio [39,40] at the beginning of the design to consider errors.

There are some methods for the analytical computation [41,42] of force or torque exerted on the permanent magnets in the inner or outer rotor. Although the subject of the study is based on FEM design, it is essential to reveal the relationship with the analytical results.

Virtual Work based analytical calculations are more efficacious and faster than Maxwell stress tensor and Coulombian methods.

3.1. Analytical results

The exerted force on a single-pole is calculated by the Virtual Work [43] principle as in Eq. (1) based on the stored energy change in the air gap due to the small axial displacement between the poles. Similarly, the torque can be calculated if the axial displacement (x-dx) in the equation is changed with angular displacement (θ-dθ).

$$F_{single\_pole} = \frac{dW}{dx} = \frac{(B_{g1})^2 (V_{ag})}{2\mu_0 (x - dx)}; \quad T = \frac{dW}{d\theta} \tag{1}$$

where

F_{single_pole}: force exerted on a single-pole (N)
dW: change in stored energy in the air gap (J)
B_{g1}: effective air gap flux density (T) – [the 1st component]
V_{ag}: air gap volume (m^3)
μ_0: free space permeability (4*pi*10^-7 H/m)
x: pole arc length (m)
dx: small displacement distance of a pole (m)
T: torque exerted on a single-pole (N)

However, if the force acting on a pole and the small displacement distance are known, the required air gap volume is found together with the assumption of the air gap magnetic flux density, which is initially chosen as 0.6 T to keep PMs away from demagnetisation. Hence, the analytical calculations summarised in Table 2 are based on the critical angle, in which case (x-dx) is directly equal to dx and similarly (θ-dθ) is directly equal to dθ. θ and dθ are the mechanical angle of a pole and small angular displacement in radians, respectively.

Fig. 6 shows the parameter definitions for the Virtual Work calculations. The air gap volume is the volume between the inner diameter of the outer rotor and the outer diameter of the inner rotor.

If the inner rotor is to be mounted directly on the piston engine shaft, the inner diameter of the inner rotor (r_{in}) can be at least 42 mm, as shown in Fig. 2(a). The effective air gap is the middle of the air gap. The effective air gap radius ($r_{effective}$) is conventionally used in place of the inner or outer magnet radius in analytical calculations of force or torque on the rotors, as shown in Fig. 6. Considering the thickness of the inner rotor yoke and magnets, as shown in Fig. 2(b), $r_{effective}$ is initially selected as 30 mm. The thickness of the sleeve is experientially assumed to be 0.5 mm. Accordingly, the total air gap clearance with the air gap is

Table 2
Analytical calculations for initial sizing.

Virtual Work Method Output	**Analytical Virtual Work Method**	
	8-pole	**10-pole**
Air gap volume, required	3427 mm^3	2192 mm^3
Length of the model, required	12.12 mm	7.75 mm
(x-dx), equals dx at critical angle	11.78 mm	9.42 mm
(θ-dθ), equals dθ at critical angle	0.3925 rad.	0.314 rad.
Critical angle	22.5 (Mdeg)	18 (Mdeg)
Force on EAG based on a single pole	41.67 N	33.33 N
Total force on EAG based on total pole number	333.33 N	
Preliminary Design Assumptions		
Effective air gap radius		30 mm
Average air gap flux density		0.6 T
Air gap length/Retaining sleeve thickness		1/0.5 mm
Pullout torque, required		10 N·m
Magnet grade		N48H-60deg

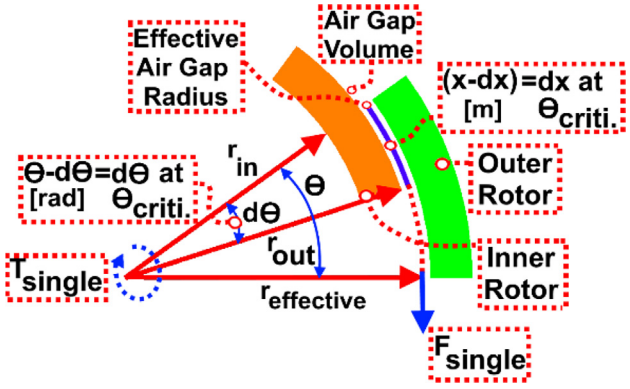

Fig. 6. Parameter definition for Virtual Work method calculations.

1.5 mm. Thus, the corresponding inner rotor outer diameter and outer rotor inner diameter are found to be 29.25 mm and 30.75 mm, respectively.

The critical angle ($\theta_{critical,Mdeg}$) [44–45], calculated as in Eq. (2), is the angle at which pullout torque is obtained and corresponds to the electrical angle (θ_{Edeg}) of 90°. Mdeg and Edeg represent the mechanical and electrical degrees, respectively. (2p) is the total number of poles. θ and $\theta_{critical}$ are 36 Mdeg and 18 Mdeg for 10-poles, and 45 Mdeg and 22.5 Mdeg for 8-poles, respectively. The corresponding θ and dθ at the critical angle in radians in Fig. 6 are 0.628 and 0.314 for 10-poles, and 0.785 and 0.3925 for 8-poles, respectively.

$$\theta_{critical,Mdeg} = \frac{360^{\circ}}{(2p)*2}; \quad \theta_{Edeg} = \frac{(2p)}{2} * \theta_{Mdeg} \tag{2}$$

Similarly, the pole arc-length and small displacement distance at the critical angle are found to be 18.85 mm and 9.42 mm for 10-poles, and 23.56 mm and 11.78 mm for 8-poles, respectively. On the other hand, the total force is the force exerted on the Effective Air Gap (EAG) used to calculate the force on the rotors in light of the total number of poles. Since the required torque is 10 N·m, the ideal total force is calculated as 333.33 N by determining the $r_{effective}$. Hence, the force exerted on a single-pole is 33.33 N for 10-poles and 41.67 N for 8-poles, respectively. The respective air gap volume is calculated as 2192 mm^3 for 10-poles and 3427 mm^3 for 8-poles. Thus, the required model length is found to be 7.75 mm for 10-poles and 12.12 mm for 8-poles, as seen in Table 2.

3.2. Maxwell 2D magnetostatic optimetric design based on FEA

Maxwell 2D solutions are based on optimetric assignments and sensitivity tools. The magnetic coupling model is fully parameterised for multiparameter analyses to explore the effect of variables. FEM is a powerful and precise tool for calculating the transferrable maximum or pullout torque at the critical angle. Maxwell 2D becomes error-reduced by close to 10% by applying more mesh in critical areas such as the air gap, as shown in the model mesh distribution in Fig. 7(a). Maxwell 2D analyses are considered in the solution type of transient in the dynamic state and magnetostatic in the static state.

Fig. 7(b) illustrates the pole embrace and offset, which are set to 0.98 and 0, respectively, for ease of assembly and manufacturability needs. Embrace is defined as the ratio of pole arc to pole pitch, while offset defines the concentricity of permanent magnets.

3.2.1. Investigation of pullout torque in outer diameter and length

Design sizing should start from the outer rotor towards the inner rotor, unlike the conventional method, due to outer rotor outer diameter limitations. In Fig. 8(a), the coupling length and the outer rotor outer diameter are varied to explore the pullout torque. The outer rotor assignments range from a maximum possible outer diameter of 74 mm to a minimum possible outer diameter of 66 mm at the critical angle based on the number of poles 10. The coupling length varies between 9 mm and 13 mm. The torque density depending on the outer rotor outer diameter at a coupling length of 10 mm is analysed in Fig. 8(b).

In Figs. 8(a) and 8(b), the thicknesses of the PMs, rotor yokes, retaining sleeve and air gap length are set to 4 mm, 4 mm, 0.5 mm and 1 mm, respectively. The minimum possible inner diameter of the inner rotor is 31 mm, considering the mounting points. The minimum corresponding outer diameter of the inner rotor yoke is 39 mm and the inner diameter of the outer rotor PMs is 50 mm. However, since the maximum torque density is obtained at the maximum outer rotor outer diameter, as shown

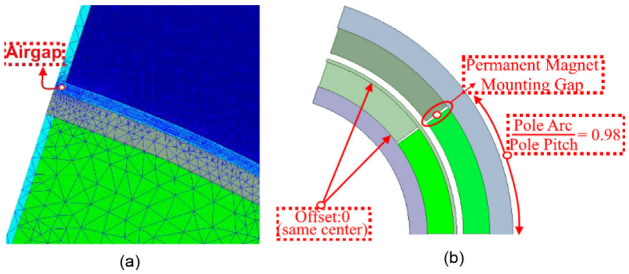

Fig. 7. Definition of (a) Mesh distribution (b) pole embrace and pole arc offset.

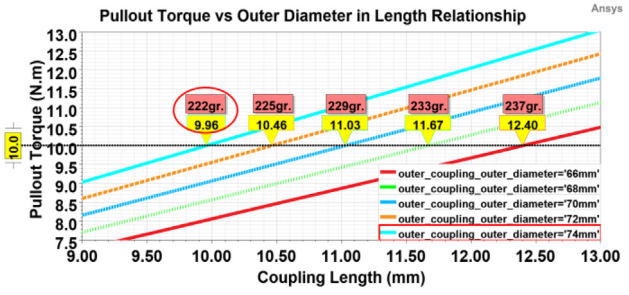

Fig. 8a. Pullout torque in outer diameter and length.

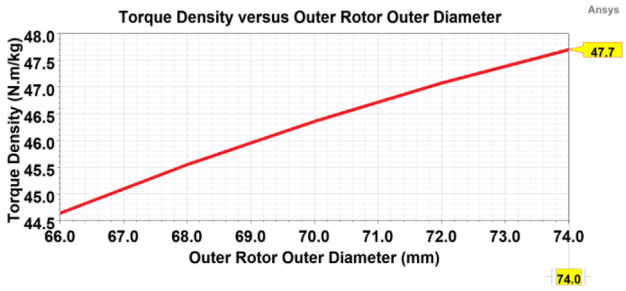

Fig. 8b. Torque density depending on the outer diameter of the outer rotor.

in Fig. 8(b), an outer diameter of 74 mm and a corresponding length of 10 mm are chosen.

On the other hand, keeping the outer diameter of the outer rotor close to the limits contributes positively to the operation of the piston engine by increasing the mechanical strength and flywheel effect.

3.2.2. Determination of PM thickness based on the static pullout torque

Static torque refers to the torque of the MC in the locked-rotor state, also called locked-rotor torque. Fig. 9 examines the static pullout torque corresponding to different thicknesses of inner and outer rotor permanent magnets. It is observed that the required torque can be achieved at different magnet thicknesses.

However, a thickness of 4 mm is preferred for the inner and outer permanent magnets, as marked in red in Fig. 9, where the required torque is provided with ease of assembly and classification.

3.2.3. Investigation of locked-rotor torque depending on torque angle

The torque angle is expressed as the mechanical angle between the inner and outer rotor d-axes at the time the magnetic coupling is being loaded. It defines transferable torque by the magnetic couplings and determines the overload capacity of the system. Fig. 10 explores the locked-rotor torque depending on the torque angle variation.

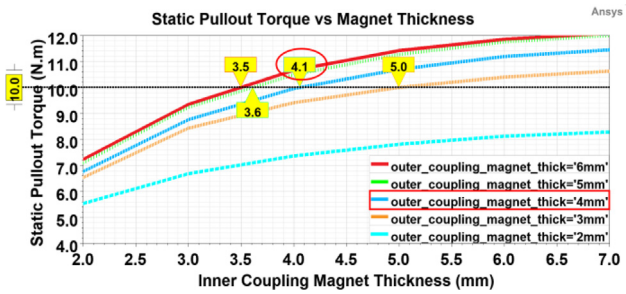

Fig. 9. Static pullout torque with respect to changes in PM thickness.

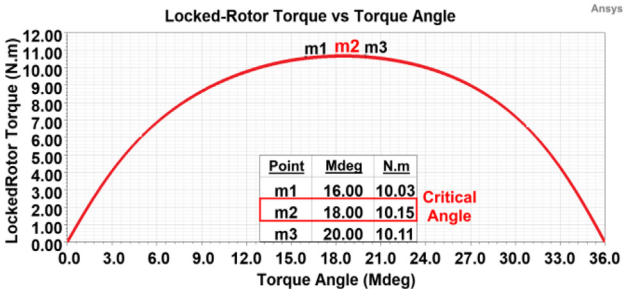

Fig. 10. Locked-rotor torque depending on torque angle.

The maximum torque of 10.15 N·m is obtained at the critical angle, satisfying the torque requirement of the design. Magnetic couplings are expected to operate close to the point of critical angle to achieve high torque density. However, in this case, any turbulence may cause the coupling to be out of synchronisation. In aviation, the pullout torque should be provided slightly below the critical angle, or coefficients should be determined that consider turbulence effects.

3.2.4. Determination of the thickness of rotor yokes

The thickness of the rotor yokes directly affects the torque as it changes the average air gap flux density by affecting the total reluctance. In addition, due to the outer diameter limitation, the rotor yokes determine the effective air gap radius, which affects the torque density by varying the inner and outer rotor diameters.

The thicknesses of the outer and inner rotor yokes are found to be 3.5 mm and 3 mm, respectively, as marked in red in Fig. 11 since the minimum thickness of the rotor yokes meeting the pullout torque requirement results in the minimum coupling weight. On the other hand, in yokeless design, where the use of magnetic materials is prohibited, the same torque can only be achieved with thicker PMs.

The magnetic flux density and the magnetic flux distribution are investigated in Fig. 12(a) and (b), respectively. Further efforts would be adopted for the embrace and magnet housing to reduce leakage fluxes, as marked in red in Fig. 12(b). However, the yoke materials of Steel 1020 could be utilised better than the electrical steels for rotor yokes in magnetic coupling applications due to its high saturation level of 2.5 T. Working at saturation points does not always mean higher torque density, but it can mean the lowest weight. Thus, the air gap flux density at no-load and full-load conditions is analysed in Fig. 13. It decreases as the coupling is loaded but is far from the point of PM saturation.

3.2.5. Investigation of the model length of magnetic coupling

Due to the outer diameter limitation, the length must be increased to obtain higher torque, allowing modular operation. A

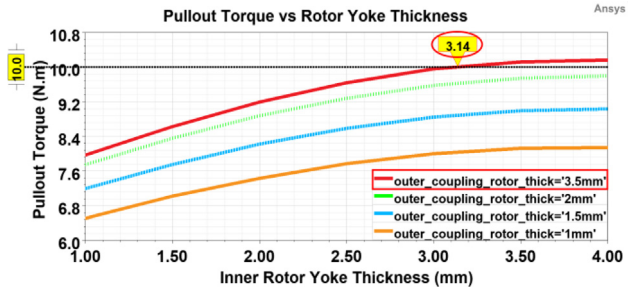

Fig. 11. Pullout torque with respect to changes in rotor yoke thickness.

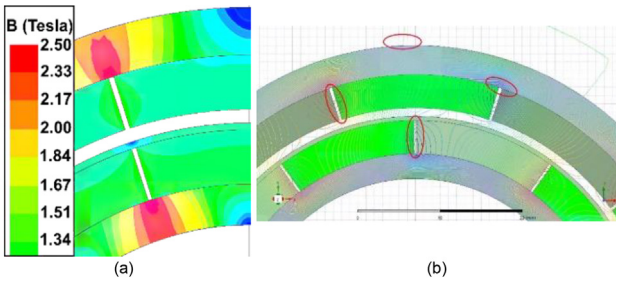

Fig. 12. (a) Flux density of rotor yokes (b) flux distribution for the 10-pole configuration.

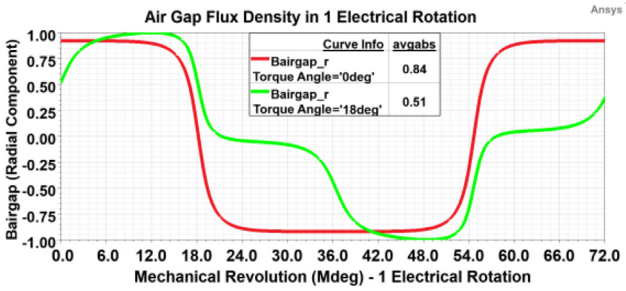

Fig. 13. Air gap flux density distribution at no-load and full-load.

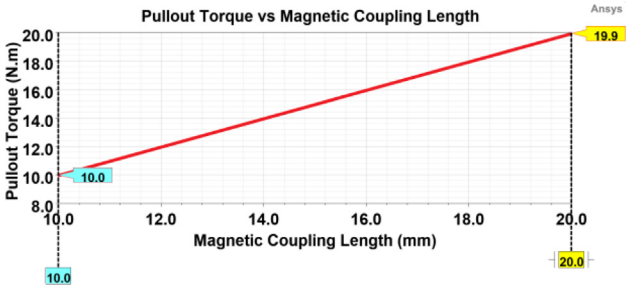

Fig. 14. Pullout torque depending on coupling length.

twofold increase in length corresponds to almost a twofold increase in torque, as shown in Fig. 14. Thus, the second MC is achieved with a model length of 20 mm.

3.2.6. Number of poles determination based on pullout torque

In synchronous MCs with a 1:1 speed conversion ratio, the number of rotor poles is equal. Increasing the pole number increases the torque as it increases the air gap flux density up to the point where leakage fluxes dominate. The mounting and weight reduction holes in the rotor also affect the number of poles where the maximum torque is obtained.

As shown in Fig. 15, the pullout torque is obtained when the number of poles is 18. However, the increase in the pole number also means an increase in the difficulty of mounting, especially the outer rotor magnets. Therefore, the number of poles is chosen as 10, as it minimally meets the system torque and weight requirements. If 8 poles are to be used, the model length should be increased by 20% to achieve the required torque, which would increase the total weight by approximately 23%.

3.3. Design of retaining sleeve or bandage

At speeds above 3600 rpm, so-called high speed, the use of a retaining sleeve is required to prevent magnets from leaving the

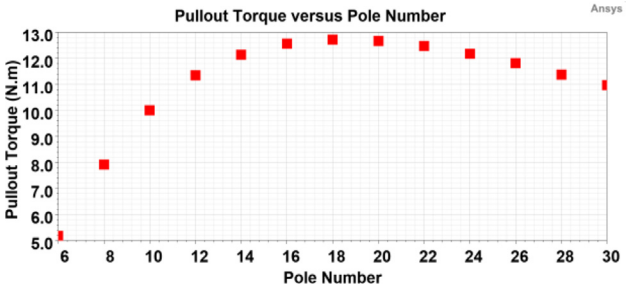

Fig. 15. Pullout torque depending on the number of poles.

Table 3
Properties of Steel316L used in analytical design of retaining sleeve.

Mass density	8000	kg/m^3
Tensile strength, ultimate/yield	515/205	MPa
Young's modulus (Elasticity modulus)	193,000	MPa
Poisson's ratio	0.25	
Magnetic permeability	1.02	

rotor surface due to high centrifugal force. Nonmagnetic stainless steel 316L, whose properties are listed in Table 3, is often used as the sleeve material. Although the sleeve thickness could be determined quickly by optimetric analyses in Maxwell 2D, analytical calculations based on centrifugal pressure and tangential stress [46] could be performed to estimate the preliminary dimensions. The analytical results based on the inner rotor dimensions shown in Fig. 16(a) are summarised in Table 4 and verified by Ansys structural analysis, as shown in Fig. 16(b).

3.3.1. Analytical design of the retaining sleeve

The minimum sleeve thickness is the thickness that provides the following fundamental two conditions when the adhesive is neglected.

1. Residual contact pressure between the magnets and the rotor core at overspeed must be positive, as given in Eq. (3).

$$p_c = (p_{c,\text{prestress}} - p_{w,m} - p_{w,b}) > 0 \tag{3}$$

where $p_{w,b}$: centrifugal force on sleeve shell *MPa*

$p_{w,m}$: centrifugal force on magnets *MPa*
$p_{c,prestress}$: contact pressure due to interference fit of sleeve onto magnets fundamental two conditions when the adhesive *MPa*
p_c : *residualcontactpressure MPa*

The centrifugal forces on the sleeve and magnets reducing residual contact pressure are given in Eqs. (3a) and (3b), respectively.

$$p_{w,b} = r_b * \rho_b * w^2_{overspeed} * h_b \tag{3a}$$

where $p_{w,b}$: centrifugal force on sleeve *MPa*

r_b : *mean radius of sleeve shell m*
ρ_b : *mass density of sleeve shell kg/m^3*
$w_{overspeed}$: *angular velocity, at over speed rad/s*
h_b : *thickness of sleeve shell m*

$$p_{w,m} = r_m * \rho_m * w^2_{overspeed} * h_m \tag{3b}$$

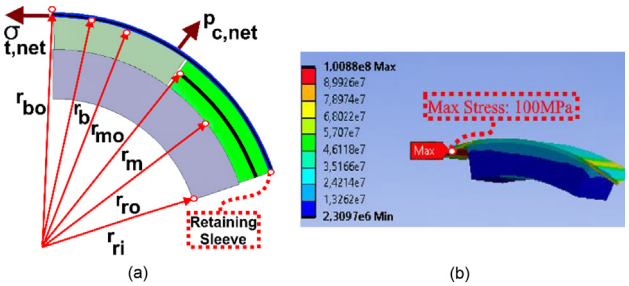

Fig. 16. (a) Inner rotor parameter definitions (b) Ansys structural sleeve verification.

Table 4
Summary of the analytical design of the retaining sleeve.

DESIGN INPUTS			
r_{ri}	Inner radius of inner rotor	21	mm
r_{ro}	Outer radius of inner rotor	24	mm
r_m	Mean radius of permanent magnet	26	mm
r_{mo}	Outer radius of permanent magnet	28	mm
r_b	Mean radius of retaining sleeve	28.25	mm
r_{bo}	Outer radius of retaining sleeve	28.5	mm
ΔD	Sleeve undersize	0.1	mm
γ_{over}	Overspeed factor	1.5	
γ_{safety}	Safety factor	2	
DESIGN OUTPUTS			
Residual Contact Pressure at Overspeed			
Centrifugal force on sleeve	$p_{w,b}$	0.14	MPa
Centrifugal force on a magnet	$p_{w,m}$	1.01	MPa
Contact pressure due to interference fit of sleeve	$p_{c,prestress}$	6.27	MPa
Residual contact pressure	p_c	5.12	MPa
Stress Inside Retaining Sleeve Shell			
Tangential stress due to rotation of sleeve	$\sigma_{t,w}$	8.17	MPa
Prestress due to interference fit of sleeve	$\sigma_{t,prestress}$	354	MPa
Stress inside retaining sleeve shell	σ_t	362	MPa
Determination of Retaining Sleeve Thickness			
Minimum required thickness of retaining sleeve, based on contact pressure	$h_{b,min,pressure}$	0.24	mm
Minimum required thickness of retaining sleeve, based on tangential stress	$h_{b,min,stress}$	0.28	mm
Selected thickness of retaining sleeve	$h_{b,selected}$	0.5	mm

where $p_{w,m}$: centrifugal force on magnet *MPa*

r_m : *mean radius of magnets m*
ρ_m : *mass density of magnets* kg/m^3
h_m : *thickness of magnets m*

The contact pressure and prestress due to the interference fit of the sleeve shell onto the magnets are evaluated by Eqs. (3c) and (3d).

$$p_{c,prestress} = \sigma_{t,prestrees} * \frac{(r_{bo}^2 - r_{mo}^2)}{(r_{bo}^2 + r_{mo}^2)} \quad (3c)$$

where $\sigma_{t,prestrees}$: prestress due to interference fit of sleeve onto magnets *MPa*

r_{bo} : *sleeve shell outer radius m*
r_{mo} : *magnet outer radius m*

$$\sigma_{t,prestrees} = E * \frac{\Delta D}{2 * r_b} \quad (3d)$$

where E : Young's modulus *MPa*

ΔD : *sleeve undersize m*

2. The stress inside the retaining sleeve must be less than the maximum endurable tangential stress, as given in Eq. (4).

$$\sigma_t = (\sigma_{t,prestrees} + \sigma_{t,w}) < \sigma_{t,max} \quad (4)$$

where $\sigma_{t,w}$: tangential stress due to sleeve rotation *MPa*

$\sigma_{t,max}$: maximum tangential stress *MPa*
σ_t : *stressinsideslee veshell MPa*

The tangential stress due to rotation of the retaining sleeve shell with a mass density of ρ_b can be estimated as in Eq. (4a) [47].

$$\sigma_{t,w} = \rho_b * w_{overspeed}^2 * r_b^2 \quad (4a)$$

The residual contact pressure at overspeed, p_c, is positive, and the stress inside the retaining sleeve, σ_t, is less than the ultimate tensile stress of the sleeve, as seen in Table 3. Similarly, the tensile stress in the sleeve obtained by numerical Ansys structural analysis is below the ultimate tensile stress of Steel316L material, as shown in Fig. 16(b).

Analytical equations are interpolated by increasing the sleeve thickness starting from 0.05 mm with 0.05 mm step intervals. The minimum sleeve thickness satisfying the above conditions is found to be 0.24 mm for contact pressure and 0.28 mm for tangential stress, considering the safety factor. However, it is difficult to find or process material with such a thin thickness. From a production point of view and a safety factor of 2, a sleeve thickness of 0.5 mm is a practical choice.

3.3.2. Investigation of eddy-current loss depending on sleeve thickness

The retaining sleeve thickness should be chosen carefully because it changes the air gap length, the torque density and the induced eddy-current losses. Eddy-current losses should be studied in detail as they increase the magnet temperature, causing a decrease in the magnet residual flux density. The maximum magnet temperature is analysed as 30 °C with numerical Ansys Fluent. As shown in Fig. 17, the induced eddy-current loss increases as the retaining sleeve thickness increases. The optimetric analysis is based on the total air gap clearance, which is the sum of the 1 mm air gap length and the sleeve thickness.

3.4. Maxwell 2D transient optimetric analyses

Unlike the magnetostatic simulations, the Ansys Maxwell transient simulation environment is created for the dynamic case, where the moment of inertia of the magnetic coupling, mechanical losses as damping factors, and the type of load acting are considered.

For more realistic analyses, the model is constructed in Solidworks, and the corresponding moments of inertia for the inner and outer rotors are calculated as 0.34 kg·cm^2 and 1.55 kg·cm^2, respectively.

The mechanical losses consisting of bearing losses, windage and friction losses are practically accepted between 2% and 4% of the output power if a CFD solution is unavailable, similar to rotating electric machines [48]. In this study, it is assumed to be 3%. The total mechanical loss is calculated as 0.000478 W/(rad/sec)^2.

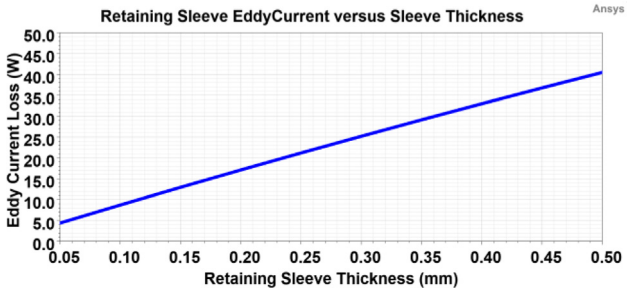

Fig. 17. Induced eddy-current loss on retaining sleeve depending on thickness.

Dynamic torque tests are performed with N48H at 60 °C due to the ease of cooling in the dynamic state. This results in a 5% higher torque per unit volume compared to static torque because the PMs have a higher residual flux density at low temperatures.

Transient simulations are performed directly at the critical angle depending on the mechanical revolutions with high-precision in low time-steps. The pullout torque with torque ripple is obtained for the case where the sleeve material is not used, as shown in Fig. 18(a). However, in the case of using a retaining sleeve, the pullout torque is reduced by approximately 10.5% due to the dominant eddy current losses, as shown in Fig. 18(b). In this case, the model length needs to be increased by approximately 12% to provide the same torque.

Due to the different moment of inertia of the rotors, dynamic torque transmission at instant load changes results in torque ripple. Figs. 18(a) and (b) show torque fluctuations of 0.1% and 0.15% for the cases without and with the sleeve, respectively, for instantaneous load variation. In synchronous magnetic couplings, the torque ripple is very small until the critical angle. Transient simulations without considering dynamic modelling result in constant torque, as shown in Fig. 18(c).

3.5. Attraction torque examination at loss of synchronisation

Investigating the torque at the Loss of Synchronisation (LoS) between coupling rotors is a critical issue in protecting the system against overloads. In aerospace applications, the system is expected to be operated by the S/G in the case of LoS. This occurs in two cases: piston shaft malfunction or exceeding the pullout torque of the MC.

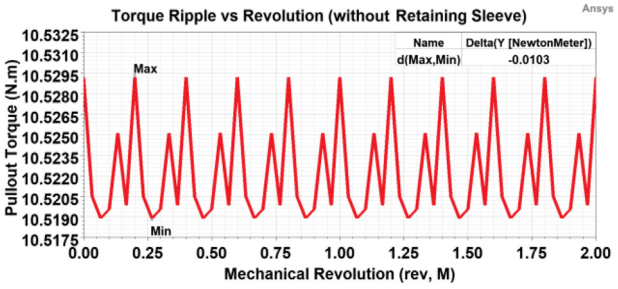

Fig. 18a. Dynamic torque without retaining sleeve at critical angle.

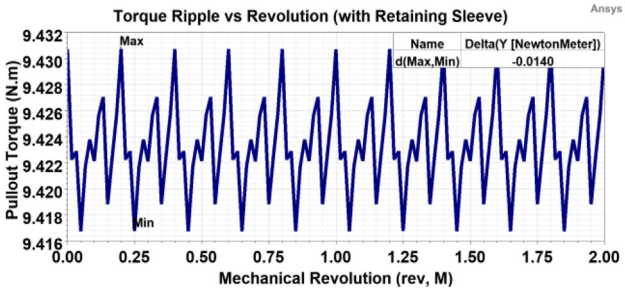

Fig. 18b. Dynamic torque with retaining sleeve at critical angle.

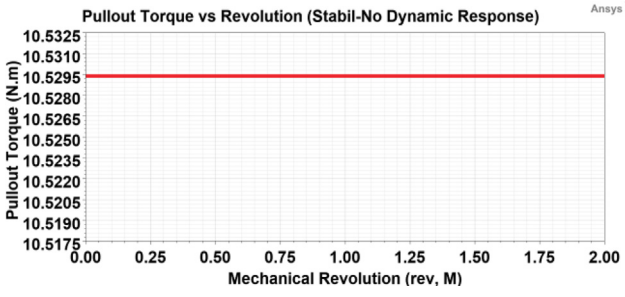

Fig. 18c. Pullout torque ignoring dynamic model at critical angle.

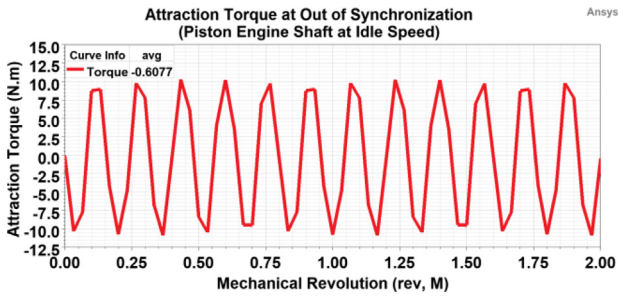

Fig. 19a. Attraction torque at out of synchronisation if piston shaft is not locked.

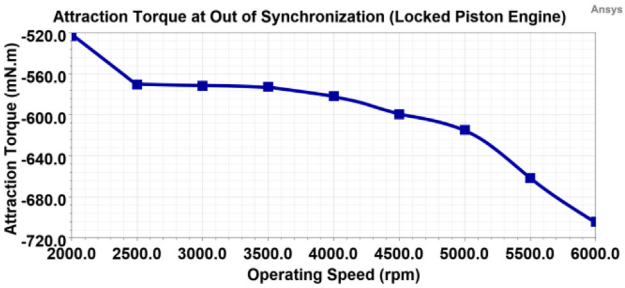

Fig. 19b. Attraction torque at out of synchronisation if piston shaft is locked.

In the case where the piston shaft is not disturbed, LoS due to overload causes the piston shaft and inner rotor of the MC to run at idle speed, 2000 rpm for 3 W-70 engine, and the outer rotor to run at near idle speed. Thus, analyses are performed under load by rotating the inner rotor at 2000 rpm and the outer rotor at 2100 rpm, just after the idle speed. Fig. 19(a) shows that the attraction torque is −0.6 N·m for this case. The effect at different speeds is further examined in Fig. 19b.

On the other hand, in case the piston engine shaft and inner rotor are locked due to any shaft failure, LoS analysis is carried out by setting the inner rotor speed to 0 and rotating the outer rotor at different operating speeds at the critical angle. As shown in Fig. 19(b), in this case, the attraction torque is −0.52 N·m for the minimum operating speed and −0.72 N·m for maximum operating speed.

The skewed model could be further studied to reduce the attraction torque [49–50], but in this case, the maximum torque per unit volume also decreases as the air gap flux density decreases.

4. Maxwell 3D parameter tuning using optimisation techniques

The optimum magnetic coupling dimensions obtained from Maxwell 2D optimetric simulations are microanalyzed using optimisation techniques in Maxwell 3D. Objectives could be the maximisation of torque per PM volume, maximisation of torque per total weight, and minimisation of cost per volume. However, a minimum weight that meets the requirements for hybrid UAV applications is often demanded.

The 3D model is split by one-fifth using symmetry features to reduce optimisation time. There are some applicable optimisation techniques [51–53] used in magnetic couplings, such as Sequential Nonlinear Programming (SNLP), Genetic Algorithm (GA), and

Multi-Objective Genetic Algorithm (MOGA). The results are summarised in Table 5.

However, the prototypes are fabricated based on the dimensions obtained from the sensitivity analyses in Table 5 since production tolerances and measurable dimensions are considered even if the maximum torque density is not provided.

4.1. Investigation of magnetic coupling efficiency and losses

It is a difficult task to analytically calculate losses, but they can be calculated numerically effectively. Magnetic coupling losses consist of rotor core losses, PM losses, sleeve losses and mechanical losses. Core losses, including hysteresis, eddy-current and excess losses, are calculated in Ansys Maxwell according to the following equation [54].

$$p_{loss} = k_h * f * B^2 + k_c * f^2 * B^2 + k_e * f^{1.5} * B^{1.5} \quad (5)$$

where k_h : *hysteresis loss coefficient of material*

f : *frequency of air gap flux density*
B : *absolute average of air gap flux density*
k_c : *eddycurrent loss coefficient of material*
k_e : *excess loss coefficient of material*

Since the inner and outer rotors rotate at the same speed in synchronous couplings, no eddy current is induced on the permanent magnets and the sleeve under ideal conditions. However, due to load disturbances, high vibration and high torque ripple from the natural operation of the piston engine, the torque angle frequently fluctuates. Thus, in addition to hysteresis losses [55], eddy-current losses [56] due to induced eddy-currents are created. These losses are converted into heat, causing the temperature of PMs to rise gradually and, if not avoided, drastically reducing the residual flux density of the PMs and the transmitted torque. Excess losses are due to the eddy current generated by the displacement of the magnetic domain walls [54].

Figs. 20(a), (b), (c), and (d) examine the rotor core losses, hysteresis losses of PMs, eddy-current losses of PMs, and eddy-current and hysteresis losses of the retaining sleeve, respectively, depending on the torque angle at the maximum operating speed for the optimum coupling of 10-poles and 10 N·m.

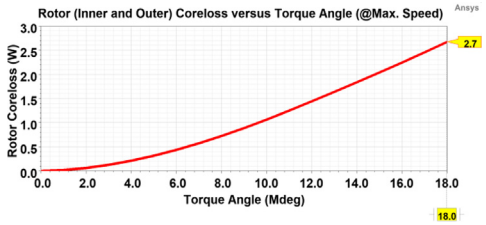

Fig. 20a. Rotor core loss depending on torque angle.

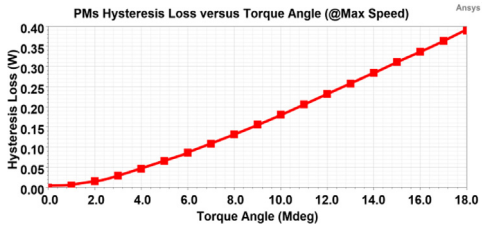

Fig. 20b. Hysteresis loss of PMs depending on torque angle.

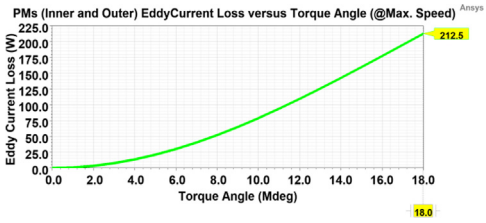

Fig. 20c. Induced eddy-current loss of PMs depending on torque angle.

In Ansys Maxwell 3D, the efficiency is analysed in two cases. In both cases, similar to Maxwell 2D, dynamic effects are included through the "Model-Motion Setup-Consider Mechanical Transient" settings. The losses and the efficiency at the critical angle for different operating speeds are obtained by keeping the inner rotor speed at zero and limiting the positive rotation of the outer rotor at different operating speeds from a torque angle of zero to the critical

Table 5
Design parameters obtained by using Maxwell 3D optimisation techniques.

Design Parameters	**Optimisation Technique**			**Sensitivity* Analyses**
	SNLP	**GA**	**MOGA**	
Inner PM thickness (mm)	4.1	4.49	4.026	4*
Outer PM thickness (mm)	3.93	4.25	3.79	4*
Inner yoke thickness (mm)	2.57	2.61	2.525	3*
Outer yoke thickness (mm)	3.03	3.02	3.028	3.5*
Optimum Model Dimensions				
Inner diameter of inner rotor (mm)	42			
Outer diameter of inner PMs (mm)	56			
Inner diameter of outer PMs (mm)	59			
Outer diameter of outer rotor (mm)	74			
Air gap volume of final model (mm^3)	2709.6			
Length of the final model (mm)	10			
Cost Function Outputs				
Average torque (N·m)	10.2	10.95	10.24	10.5
Total coupling weight (gr)	194	205	195	207
Torque density (N·m/kg)	**52.58**	**53.41**	**52.51**	**50.72**
Elapsed time (min.)	150	270	210	15

* Optimum values obtained from the sensitivity analyses.

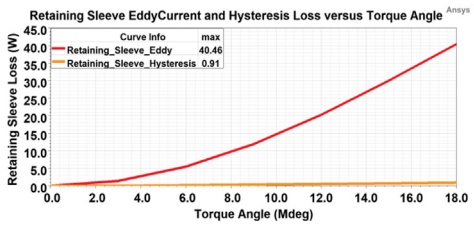

Fig. 20d. Induced eddy-current and hysteresis loss of retaining sleeve.

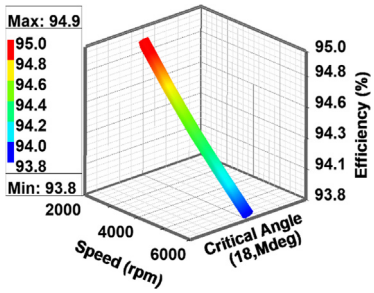

Fig. 20e. Coupling efficiency at critical angle depending on operating speed.

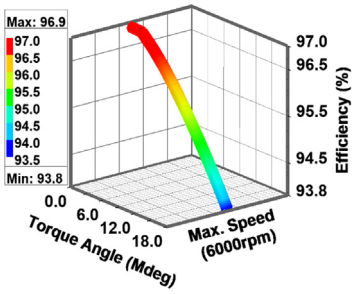

Fig. 20f. Coupling efficiency at maximum speed depending on torque angle.

angle. The losses and the efficiency at the maximum operating speed for different torque angles are obtained by keeping the inner rotor speed at zero and limiting the positive rotation of the outer rotor at maximum operating speed from a torque angle of zero to the different torque angles.

Fig. 20(e) plots the respective coupling efficiency as a function of operating speed at the critical angle. Fig. 20(f) plots the efficiency as a function of torque angle at maximum operating speed. Thus, the coupling efficiency is 93.8% at the maximum speed and critical angle, while it is 96.9% at the minimum torque angle and minimum speed.

5. Test results of the magnetic couplings

It is necessary and effective to obtain the dynamic and static performance results of the magnetic couplings and compare them with simulation results. There are various methods for magnetic coupling tests, such as Direct Dynamic, Indirect Dynamic, and Static tests [27].

Static tests perform locked-rotor performance in a steady state but are deficient in calculating loss and efficiency. Indirect dynamic tests are based on estimating the pullout torque from no-load or half-load conditions with poor accuracy. However, in the direct test system, the performance results are obtained by reading the parameters such as torque, speed, and temperature using sensitive sensors, giving very accurate results. The prototypes are shown in Fig. 21. A direct-type test bench has been set up for MCs, as illustrated in Fig. 22(a). The integration of MC on a piston engine is demonstrated in Fig. 22(b,c).

5.1. Full-load dynamic test results

The test bench consists of a servo motor (1) as a load, torque/speed transmitter (2), geared asynchronous motor (3), magnetic couplings under test (4), high-speed spindle motor (5), and laser thermometer (6). If the working principle of the test system is to be explained, the magnetic coupling driven by the asynchronous motor is gradually loaded by the servo motor operating in torque mode. At the same time, the transmitted torque and speed are dynamically measured from the torque/speed sensor. The temperature of magnetic coupling is obtained with the laser thermometer. The required second coupling of 20 N·m is achieved by modularly doubling the coupling of 10 N·m in length.

Locked-rotor tests are performed by making the outer rotor of the MC unable to rotate with the first excessive torque adjustment of the servo motor. For high torque tests, the driving speed of the MCs is 250 rpm. High-speed tests are performed by spindle motor

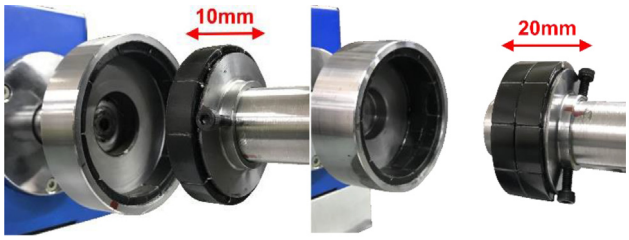

Fig. 21. Magnetic coupling prototypes with lengths of (a) 10 mm and (b) 20 mm.

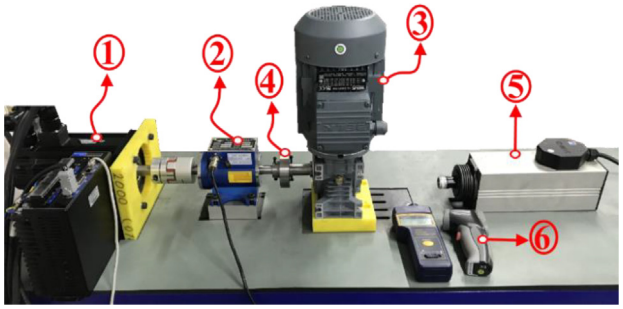

Fig. 22a. Direct dynamic test bench set up specifically for magnetic coupling tests.

Fig. 22b,c. Coupling integration on a piston engine (b) Real model (c) 3D model.

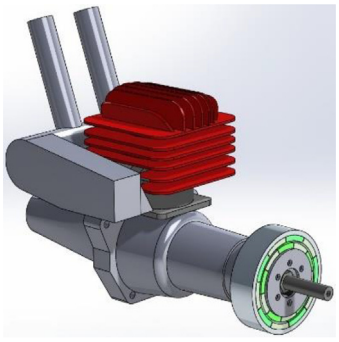

(c)

Fig. 22b,c (*continued*)

(5) on the test bench. The torque angle is measured by absolute hall encoders on the load servo motor and drive asynchronous motor. Loctite648 is used as the adhesive material for PMs, and the retaining sleeve material is omitted, but the air gap with the sleeve is left at 1.5 mm.

Although output torque and speed are measured, efficiency calculations require a second torque/speed transmitter to measure input torque and speed. Due to the lack of test facilities, efficiency could not be plotted dynamically. However, in light of the data obtained from other test results, the actual efficiency graph could be estimated from the numerical efficiency graph using the proposed correction factor.

Fig. 23(a) shows the pullout torque and temperature results obtained by the dynamic test bench for magnetic coupling with a length of 10 mm. The average pullout torque is 8.9 N·m for the dynamic tests, 10.5 N·m for transient Maxwell 2D and 9.9 N·m for transient Maxwell 3D.

Similarly, Fig. 23(b) examines the dynamic test results of the MC with a length of 20 mm. This confirms that a twofold increase in length results in almost a twofold increase in the pullout torque. Maxwell 2D and 3D transient dynamic analyses correlate strongly with the test results. Dashed lines indicate the average value of the results.

In Maxwell 3D, similar to Maxwell 2D, torque simulations in the transient dynamic state also result in torque fluctuations at sudden load changes since the moment of inertia of coupling, the mechanical losses in terms of damping factor, and the type of load acting are modelled.

3D modelling and layout of the test bench are achieved using Solidworks software to ensure precise production. The test system parts are manufactured with high precision on CNC machines and their assembly is performed by accurately measuring with reference to the 3D model. In addition, it is provided that the inner rotor of the coupling fits and rests on the bearing housing in the outer

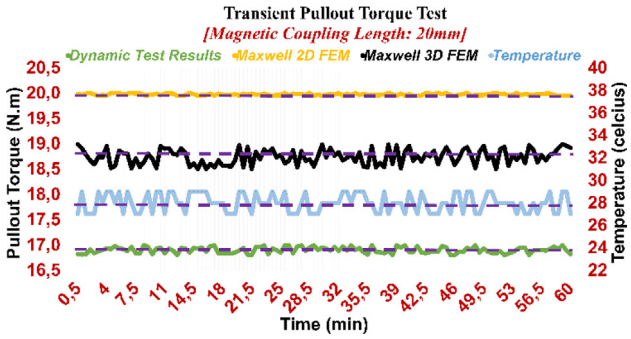

Fig. 23b. Transient pullout torque test results for MC with 20 mm length.

rotor of the coupling, ensuring that the inner and outer rotor axes are concentric and coincident. Once the assembly is assured, the parts are fixed to the platform. On the other hand, the torque/speed transmitter and temperature meter used in the tests are calibrated by an internationally accredited organisation [57]. The tests are conducted a total of three times at different times and the average values are used in the graphs.

In dynamic tests, the servo motor used in torque mode tries to continuously keep the load at the maximum torque point of the magnetic coupling according to the position information received from the encoder and current information received by the driver. However, the torque results obtained from the test bench also fluctuate due to the unstable load caused by the moment of inertia of the servo motor, the unbalanced mechanical connection between the servo and the torque sensor, and the low sensitivity of the torque sensor.

5.2. Static locked-rotor test results and correction factor determination

The locked-rotor torque results obtained from the Virtual Work method, numerical Maxwell 2D and 3D simulations and the test bench are compared in Fig. 24.

For the analytical Virtual Work method, the optimum values determined in Table 5, considering manufacturability and accessibility, were reused in Eq. (1) to calculate the torque corresponding to different torque angles. The torque increases with increasing torque angle in the synchronous zone up to the critical angle. The torque is maximum at the critical angle. In the asynchronous zone after the critical angle, the torque angle and output torque are reduced as the reference is taken from the next incoming PM with opposite polarity. However, since the system is unstable in the asynchronous region, it results in a loss of synchronisation, as investigated in Section 3.5. On the other hand, the torque is zero

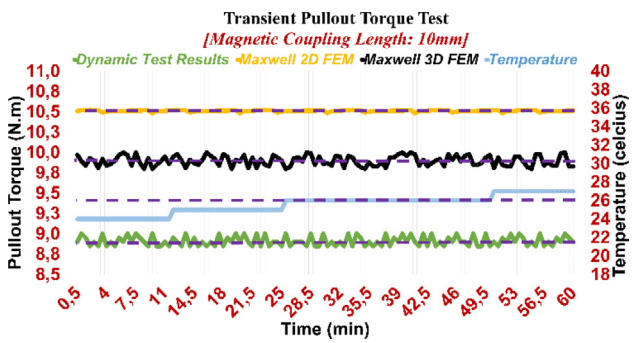

Fig. 23a. Transient pullout torque test results for MC with 10 mm length.

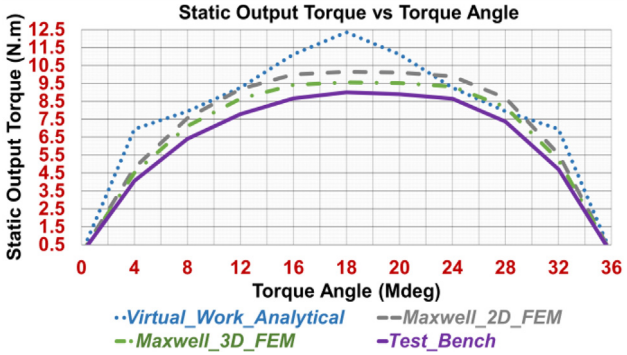

Fig. 24. Static torque results of the optimum model depending on the torque angle.

at the minimum energy position realised at the torque angle of 0 Mdeg or 36 Mdeg for the optimum model.

The locked-rotor torque at the critical angle is 9 N·m for the static tests, 10.15 N·m for static Maxwell 2D, 9.56 N·m for static Maxwell 3D, and 12.35 N·m for the Virtual Work method. The test bench static results are based on a torque angle variation of 4 mechanical degrees to reduce errors caused by torque angle reading with an absolute encoder.

To obtain more realistic results, the magnet temperature of 60 °C in the transients is updated to 80 °C in the magnetostatics due to the cooling difficulties encountered in the steady state of the system. In this way, torque deviations depending on the static and dynamic states are explored. However, since these effects cannot be created on the test bench, the static and dynamic test results are very close to each other.

Analytical methods are usually used for preliminary design of the model under ideal conditions. For this reason, calculations are mostly based on the basic parameters and the required output values. In other words, nonlinearities in the natural behaviour of the materials are not considered. For example, the effects of many variables such as leakage fluxes, cross coupling effects, core losses, thermal effects and eddy losses, are ignored in the calculations. On the other hand, analytical calculations modelling these effects are complex and time consuming. For this reason, FEM offers a practical approach for designers, and these effects are considered with high accuracy by defining the material nonlinear properties in detail and their effects on the output parameters.

Finally, the correction factor coefficient, which allows the methods used in the design to reduce errors and give results much closer to practice, can be obtained. As a result, a correction factor of 1.39 for the Virtual Work method, 1.18 for Maxwell 2D and 1.11 for Maxwell 3D is proposed by correlating analytical calculations and Maxwell FEA with the results obtained from the dynamic test system.

6. Conclusion

This article contributes to the optimum design study of active synchronous magnetic couplings with a multiobjective analysis approach. Preliminary analytical calculations are based on the Virtual Work method. The magnetic design was conducted in Ansys Maxwell 2D by optimetric solutions and in Maxwell 3D using the sensitivity analyses and the optimisation techniques of SNLP, GA, and MOGA. In light of manufacturability, a 10-pole configuration was preferred, which offers 17% higher torque density than an 8-pole configuration. The torque fluctuations are 0.1% and 0.15% for the cases without and with the retaining sleeve, respectively. The requirements are met with minimum weight by operating the system at saturation points. Calculating the attraction torque at the loss of synchronisation at an average of −0.6 N·m may indicate the necessity of skew work for S/G applications. Static structural analysis of the retaining sleeve, designed to protect permanent magnets from contact pressure and tangential stress, confirms its robustness. Magnetic couplings are produced with lengths of 10 mm and 20 mm. It has been found that a doubling of the stack length corresponds to an almost twofold increase in torque. Unlike the traditional method, the proposal of the modular stack structure provides ease of production due to the outer diameter limitation. A direct dynamic test system was installed on behalf of magnetic couplings for full load, overload, and locked-rotor tests. The dynamic and static test results are closely correlated with the Maxwell 2D and 3D FEM outputs. The experimental static results show that the absolute error of the analytical calculations is 37% for the Virtual Work method. On the other hand, the presence of errors, 13% for 2D FEM and 6% for 3D FEM, indicates the importance of numerical simulations for aviation applications. The test results can also give an idea about the safety factor and turbulence coefficient. At the critical angle, the total rotor core losses are 2.7 W, the hysteresis losses of the PMs are 0.40 W, the induced eddy-current losses on the PMs are 212.5 W, the hysteresis loss of the sleeve is 0.91 W, and the induced eddy-current loss of the sleeve is 40.46 W. Among the losses, permanent magnets and eddy current losses induced on the sleeve are predominantly effective. The coupling efficiency at the maximum operating speed and critical angle is 93.8%, while it is 96.9% at the minimum torque angle and minimum operating speed. The study provides a realistic design opportunity by including a correction factor of 1.39 for the Virtual Work method, 1.18 for Maxwell 2D and 1.11 for Maxwell 3D. Thus, it can be concluded that the modular design of synchronous radial couplings is valid and can be safely adapted to many applications.

Declaration of Competing Interest

The authors declare that they have no known competing financial interests or personal relationships that could have appeared to influence the work reported in this paper.

Acknowledgments

This work is encouraged by Promethod Engineering Ind. Trade. Co. Ltd. in Turkey. FEM analyses and optimisation are performed by using licenced use of Ansys Electronics (2D&3D) v2020R1. 3D modelling of the model is created with the licenced use of Solidworks v17.

Source of support: This work is supported in part by Türkiye Bilimsel ve Teknolojik Araştırma Kurumu (TÜBİTAK) with project number 3192296 within the scope of 1501 support program.

References

[1] W. Cao, B.C. Mecrow, G.J. Atkinson, J.W. Bennett, D.J. Atkinson, Overview of Electric Motor Technologies Used for More Electric Aircraft (MEA), IEEE Trans. Ind. Electron. 59 (2012) 3523–3531, https://doi.org/10.1109/TIE.2011.2165453.

[2] A. Griffo, R. Wrobel, P.H. Mellor, J.M. Yon, Design and Characterization of a Three-Phase Brushless Exciter for Aircraft Starter/Generator, IEEE Trans. Ind. Appl. 49 (2013) 2106–2115, https://doi.org/10.1109/TIA.2013.2269036.

[3] F. Chai, S. Cui, S. Cheng, Performance Analysis of Double-Stator Starter Generator for the Hybrid Electric Vehicle, IEEE Trans. Magn. 41 (2005) 484–487, https://doi.org/10.1109/TMAG.2004.839274.

[4] R. Ravaud, G. Lemarquand, Magnetic Couplings with Cylindrical and Plane Air Gaps: Influence of the Magnet Polarization Direction, Prog. Electromagn. Res. B 16 (2009) 333, https://doi.org/10.2528/PIERB09051903.

[5] J.P. Yonnet, S. Hemmerlin, E. Rulliere, G. Lemarquand, Analytical Calculation of Permanent Magnet Couplings, IEEE Trans. Magn. 29 (1993) 2932–2934, https://doi.org/10.1109/20.280913.

[6] R. Ravaud, G. Lemarquand, V. Lemarquand, C. Depollier, Permanent Magnet Couplings: Field and Torque Three-Dimensional Expressions Based on the Coulombian Model, IEEE Trans. Magn. 45 (2009) 1950–1958, https://doi.org/10.1109/TMAG.2008.2010623.

[7] J.Y. Choi, H.J. Shin, S.M. Jang, S.H. Lee, Torque Analysis and Measurements of Cylindrical Air-Gap Synchronous Permanent Magnet Couplings Based on Analytical Magnetic Field Calculations, IEEE Trans. Magn. 49 (2013) 3921–3924, https://doi.org/10.1109/TMAG.2013.2239265.

[8] S. Högberg, N. Mijatovic, J. Holbøll, B. B. Jensen, F. B. Bendixen, Parametric Design Optimization of a Novel Permanent Magnet Coupling using Finite Element Analysis, 2014 IEEE Energy Conversion Congress and Exposition. (2014) 1465-1471. https://doi.org/10.1109/ECCE.2014.6953591.

[9] Y. Akcay, G. Paolo, T. Oliver, G. Michael, Fast and Accurate 2D Analytical Subdomain Method for Coaxial Magnetic Coupling Analysis, Energies 14 (2021) 4656, https://doi.org/10.3390/en14154656.

[10] T. Lubin, S. Mezani, A. Rezzoug, Experimental and Theoretical Analyses of Axial Magnetic Coupling Under Steady-State and Transient Operations, IEEE Trans. Ind. Electron. 61 (2014) 4356–4365, https://doi.org/10.1109/TIE.2013.2266087.

[11] B. Ose-Zala, V. Pugachov, The Influence of Pole Pair Number and Magnets' Width on Mechanical Torque of Magnetic Coupler with Rounded Permanent Magnets, Scientific Journal of Riga Technical University, Power and Electrical Engineering. 28 (2011) 63-66, https://doi.org/10.2478/v10144-011-0011-0.

[12] K. Sun, J. Shi, W. Cui, G. Meng, Theoretical Computational Model for Cylindrical Permanent Magnet Coupling, Electronics 10 (2021) 2026, https://doi.org/10.3390/electronics10162026.
[13] Z. Meng, Z. Zhu, Y. Sun, 3-D Analysis for the Torque of Permanent Magnet Coupler, IEEE Trans. Magn. 51 (2015) 1–8, https://doi.org/10.1109/TMAG.2014.2359851.
[14] G.Y. Meng, Y.H. Niu, The Torque Research for Permanent Magnet Coupling based on Ansoft Maxwell transient Analysis, Appl. Mech. Mater. 423 (2013) 2014, https://doi.org/10.4028/www.scientific.net/AMM.423-426.2014.
[15] Y. Chen, W.N. Fu, S.L. Ho, H. Liu, A Quantitative Comparison Analysis of Radial-Flux, Transverse-Flux, and Axial-Flux Magnetic Gears, IEEE Trans. Magn. 50 (2014) 1–4, https://doi.org/10.1109/TMAG.2014.2327622.
[16] B. Dolisy, S. Mezani, T. Lubin, J. Lévêque, A New Analytical Torque Formula for Axial Field Permanent Magnets Coupling, IEEE Trans. Energy Convers. 30 (2015) 892–899, https://doi.org/10.1109/TEC.2015.2424159.
[17] K. Atallah, S.D. Calverley, D. Howe, Design, Analysis and Realisation of a High-Performance Magnetic Gear, Electric Power Applications, IEE Proc.. 151 (2004) 135–143, https://doi.org/10.1049/ip-epa:20040224.
[18] S.L. Ho, S. Niu, W.N. Fu, Transient Analysis of a Magnetic Gear Integrated Brushless Permanent Magnet Machine Using Circuit-Field-Motion Coupled Time-Stepping Finite Element Method, IEEE Trans. Magn. 46 (6) (2010) 2074–2077.
[19] S. Wang, Y.-C. Guo, P.-y. Wang, D.-Y. Li, Study on Torque Calculation for Hybrid Magnetic Coupling and Influencing Factor Analysis, 3D Res. 8 (1) (2017).
[20] J. J. Scheidler, V. M. Asnani, T. F. Tallerico, NASA's Magnetic Gearing Research for Electrified Aircraft Propulsion, 2018 AIAA/IEEE Electric Aircraft Technologies Symposium (EATS). (2018) 1-12, https://doi.org/10.2514/6.2018-4988.
[21] T. F. Tallerico, J. J. Scheidler, Z. A. Cameron, Electromagnetic Mass and Efficiency of Magnetic Gears for Electrified Aircraft, 2019 AIAA/IEEE Electric Aircraft Technologies Symposium (EATS). (2019) 1-25, https://doi.org/10.2514/6.2019-4475.
[22] M. Benarous, M. Trezieres, Design of a Cost-Effective Magnetic Gearbox for an Aerospace Application, J. Eng. 2019 (2019) 4081–4084, https://doi.org/10.1049/joe.2018.8238.
[23] T. F. Tallerico, Z. A. Cameron, J. J. Scheidler, Design of a Magnetic Gear for NASA's Vertical Lift Quadrotor Concept Vehicle, 2019 AIAA/IEEE Electric Aircraft Technologies Symposium (EATS). (2019) 1-21, https://doi.org/10.2514/6.2019-4477.
[24] G. Puchhammer, Magnetic Gearing versus Conventional Gearing in Actuators for Aerospace Applications, Proceeding of the 42nd Aerospace Mechanisms Symposium, NASA Goddard Space Flight Center, 2014.
[25] J.F. Charpentier, N. Fadli, J. Jennane, Study of Ironless Permanent Magnet Devices being both a Coupling and an Axial Bearing for Naval Propulsion, IEEE Trans. Magn. 39 (2003) 3235–3237, https://doi.org/10.1109/TMAG.2003.816732.
[26] R. Bojoi, A. Cavagnino, A. Miotto, A. Tenconi, S. Vaschetto, Radial Flux and Axial Flux PM Machines Analysis for More Electric Engine Aircraft Applications, 2010 IEEE Energy Conversion Congress and Exposition. (2010) 1672-1679, https://doi.org/10.1109/ECCE.2010.5618110.
[27] "IEEE Approved Draft Trial-Use Guide for Testing Permanent Magnet Machines," in IEEE P1812/D5, July 2014 , vol., no., pp.1-65, 14 Dec. 2014.
[28] S.M. Huang, W.L. Chen, C.H. Yau, C.K. Sung, Effects of misalignment on the transmission characteristics of magnetic couplings, Proc. Inst. Mech. Eng. C J. Mech. Eng. Sci. 215 (2) (2001) 227–235.
[29] H. Ahn, H. Park, C. Kim, H. Lee, A Review of State-of-the-art Techniques for PMSM Parameter Identification, J. Electr. Eng. Technol. 15 (3) (2020) 1177–1187.
[30] B. Ose, V. Pugachov, S. Orlova, J. Vanags, The Influence of Permanent Magnets' Width and Number on the Mechanical Torque of a Magnetic Coupler with Rectangular Permanent Magnets, 2011 IEEE International Symposium on Industrial Electronics. (2011) 761, https://doi.org/10.1109/ISIE.2011.5984253.
[31] A.J. Fard, M. Mirsalim, An Adaptive Method for Calculation of Iron Losses in Switched Reluctance Motors using a Minimum Number of Magnetostatic Finite Element Simulations, COMPEL-The international journal for computation and mathematics in electrical and electronic engineering. 41 (2022) 1566–1583, https://doi.org/10.1108/COMPEL-07-2021-0251.
[32] K.-C. Min, H.-B. Kang, M.-G. Park, H.-W. Cho, J.-Y. Choi, Eddy Current Loss Analysis in Radial Flux type Synchronous Permanent Magnet Coupling using Space Harmonic Methods, Trans. Korean Inst. Electr. Eng. 63 (10) (2014) 1377–1383.
[33] S. Kanazawa, N. Takahashi, T. Kubo, Measurement and Analysis of AC Loss of NdFeB Sintered Magnet, IEEJ Trans. Fundam. Mater. 124 (2004) 869–875, https://doi.org/10.1002/eej.20213.
[34] S. Arslan, I. Iskender, Design Aspects of a 26500-Rpm 2-kW High-speed Permanent Magnet Synchronous Generator for Turbomachinery Systems, 8th International Conference on Electronics, Computers and Artificial Intelligence (ECAI). (2016) 1-6, https://doi.org/10.1109/ECAI.2016.7861084.
[35] W.Q. Yuan, Y. Liu, D. Li, G.Y. Meng, Research on Overloading Protection of Permanent Magnetic Coupler in Coal Mine, Appl. Mech. Mater. 597 (2014) 492, https://doi.org/10.4028/www.scientific.net/AMM.597.492.
[36] A. Matthee, Development of a Magnetic Gear for Dry-Cooling Power Plant Applications, Department of Electrical and Electronic Engineering, University of Stellenbosch, 2017 (M.Sc. Dissertation).
[37] X. Sun, Q. Hu, L. Yan, Y. Chen, K. Zhang, J. Qu, A Magnetic Torque Optimization Method for a Hydraulic-Magnetic Coupling-Drive Cuttings Cleaning Tool, Nat. Gas Ind. B 6 (2019) 374–383, https://doi.org/10.1016/j.ngib.2019.01.013.
[38] S.H. Kim, J.W. Shin, K. Ishiyama, Magnetic Bearings and Synchronous Magnetic Axial Coupling for the Enhancement of the Driving Performance of Magnetic Wireless Pumps, IEEE Trans. Magn. 50 (2014) 1–4, https://doi.org/10.1109/TMAG.2013.2278837.
[39] M.H. Gozin, M. Aghaie-Khafri, 2D and 3D Finite Element Analysis of Crack Growth under Compressive Residual Stress Field, Int. J. Solids Struct. 49 (2012) 3316–3322, https://doi.org/10.1016/j.ijsolstr.2012.07.014.
[40] W. Wu, H.C. Lovatt, J.B. Dunlop, Analysis and Design Optimisation of Magnetic Couplings using 3D Finite Element Modelling, IEEE Trans. Magn. 33 (1997) 4083–4094, https://doi.org/10.1109/20.619670.
[41] R. Ravaud, V. Lemarquand, G. Lemarquand, Analytical Design of Permanent Magnet Radial Couplings, IEEE Trans. Magn. 46 (2010) 3860–3865, https://doi.org/10.1109/TMAG.2010.2056379.
[42] O. Bíró, A. Bossavit, Virtual Power Principle and Maxwell's tensor: Which comes first?, Compel-the Int J. Comput. Math. Electr. Electron. Eng. 30 (6) (2011) 1804–1814.
[43] M. Nagrial, J. Rizk, A. Hellany, Design of Synchronous Torque Couplers, World Academy of Science, Engineering and Technology, Open Science Index 55, Int. J. Mech. Mechatron. Eng. 5 (2011) 1319–1324, https://doi.org/10.5281/zenodo.1077689.
[44] B. Ose-Zala, V. Pugachov, The Comparison of Active and Reactive Magnetic Couplers, 2012 Electric Power Quality and Supply Reliability. (2012) 1-4. https://doi.org/10.1109/PQ.2012.6256194.
[45] B. Ose-Zala, O. Onzevs, V. Pugachov, Formula Synthesis of Maximal Mechaical Torque on Volume for Cylindrical Magnetic Coupler, Electrical, Control and Communication Engineering. 3 (2013) 37-43, https://doi.org/10.2478/ecce-2013-0013.
[46] W. Zhao, X. Wang, C. Gerada, H.e. Zhang, C. Liu, Y. Wang, Multi-Physics and Multi-Objective Optimization of a High Speed PMSM for High Performance Applications, IEEE Trans. Magn. 54 (11) (2018) 1–5.
[47] A. Binder, T. Schneider, M. Klohr, Fixation of Buried and Surface Mounted Magnets in High-Speed Permanent Magnet Synchronous Motors, Fourtieth IAS Annual Meeting. Conference Record of the 2005 Industry Applications Conference. 4 (2005) 2843-2848, https://doi.org/10.1109/IAS.2005.1518863.
[48] J. Pyrhönen, T. Jokinen, V. Hrabovcová, Design of Rotating Electrical Machines, John Wiley & Sons: United Kingdom 2014.
[49] N. Niguchi, K. Hirata, Cogging Torque Analysis of Magnetic Gear, IEEE Trans. Ind. Electron. 59 (2012) 2189–2197, https://doi.org/10.1109/TIE.2011.2159357.
[50] H. Zaytoon, A. S. Abdel-Khalik, S. Ahmed, A. Massoud, Cogging Torque Reduction of Axial Magnetic Gearbox using Pole Pairing Technique, 2015 IEEE International Conference on Industrial Technology (ICIT). (2015) 652-657, https://doi.org/10.1109/ICIT.2015.7125172.
[51] A. Canova, F. Freschi, G. Gruosso, B. Vusini, Genetic Optimisation of Radial Eddy Current Couplings, COMPEL-Int. J. Comput. Math. Electr. Electron. Eng. 24 (2005) 767–783, https://doi.org/10.1108/03321640510598120.
[52] W. Yu Lin, L. Pin Kuan, W. Jun, D. Han, Near-Optimal Design and 3-D Finite Element Analysis of Multiple Sets of Radial Magnetic Couplings, IEEE Trans. Magn. 44 (12) (2008) 4747–4753.
[53] L. Jian, G. Xu, J. Song, H. Xue, D. Zhao, J. Liang, Optimum Design for Improving Modulating Effect of Coaxial Magnetic Gear Using Response Surface Methodology and Genetic Algorithm, Prog. Electromagn. Res.-pier. 116 (2011) 297–312, https://doi.org/10.2528/PIER11032316.
[54] Maxwell Help Core Loss Coefficients, Release 20.1, Ansys® Electronics, 2020, pp. 906-908.
[55] D. Egorov, I. Petrov, J.J. Pyrhonen, J. Link, R. Stern, P. Sergeant, B. Sarlioglu, Hysteresis Loss in NdFeB Permanent Magnets in a Permanent Magnet Synchronous Machine, IEEE Trans. Ind. Electron. 69 (1) (2022) 121–129.
[56] D. Ouamara, F. Dubas, Permanent-Magnet Eddy-Current Losses: A Global Revision of Calculation and Analysis, Math. Comput. Appl. 24 (2019) 67, https://doi.org/10.3390/mca24030067.
[57] Ums Quality Electrical Calibration Co. Ltd. Home Page. Available online: https://www.umskalite.com (accessed on 13 February 2023).